Chemical Engineering Journal 286 (2016) 369–376

Contents lists available at ScienceDirect

Chemical Engineering Journal

journal homepage: www.elsevier.com/locate/cej

Efficient ceria–silica catalysts for BTX oxidation: Probing the catalytic performance and oxygen storage

Anderson G.M. da Silva [a], Humberto V. Fajardo [b], Rosana Balzer [c], Luiz F.D. Probst [c], Nayara T. Prado [d], Pedro H.C. Camargo [a], Patricia A. Robles-Dutenhefner [d,*]

[a] Departamento de Química Fundamental, Instituto de Química, Universidade de São Paulo, Av. Prof. Lineu Prestes, 748, 05508-000 São Paulo, SP, Brazil
[b] Departamento de Química, Universidade Federal de Ouro Preto, 35400-000 Ouro Preto, MG, Brazil
[c] Departamento de Química, Universidade Federal de Santa Catarina, 88040-900 Florianópolis, SC, Brazil
[d] Departamento de Química, Universidade Federal de Minas Gerais, 31270-901 Belo Horizonte, MG, Brazil

HIGHLIGHTS

- CeO_2 based catalysts were prepared by impregnation method and MCM-41 supports.
- The method of preparation affects the dispersion/incorporation of the CeO_2 which led to higher catalytic activities.
- CeO_2–MCM-41 material showed better BTX oxidation capacity.

ARTICLE INFO

Article history:
Received 30 July 2015
Received in revised form 27 October 2015
Accepted 30 October 2015
Available online 4 November 2015

Keywords:
BTX oxidation
Ceria–silica catalyst
MCM-41

ABSTRACT

This paper describes a systematic investigation on the synthesis of CeO_2 supported on SiO_2 by two different methods: (i) the in situ incorporation of CeO_2 onto MCM-41 and (ii) wet impregnation. We were interested in investigating how the CeO_2 preparation could influence their physicochemical properties and catalytic performances towards the benzene, toluene, and *o*-xylene (BTX) oxidation reactions. Our results showed that the catalytic performances were strongly dependent on the synthetic approach, in which the CeO_2–MCM-41 material prepared by the in situ incorporation showed better BTX oxidation activities than the CeO_2-based catalysts prepared by conventional wet impregnation. This result could be assigned to the higher specific surface area, better interaction between CeO_2 and the support, improved Ce^{4+}/Ce^{3+} redox process, and higher concentration of oxygen vacancies as enabled by the in situ approach. The influence of CeO_2 content in the ordering of the SiO_2 mesoporous structure was also demonstrated.

1. Introduction

Ceria (CeO_2) is widely employed as heterogeneous catalysts towards a variety of reactions due to its interesting properties such as good oxidation–reduction potential, high oxygen storage capability (OSC), and controlled porosities [1–5]. These features play an important role in the context of CeO_2-catalyzed oxidation reactions, and originate from the easy formation and mobility of oxygen vacancies, mainly at the surface [6–9].

Especially, CeO_2 oxygen vacancies provide sites for oxygen activation and increase the diffusion rate of oxygen, that can be used to enhance catalytic processes [6,8–10]. In order to enhance the number of oxygen vacancies, many strategies have been employed such as the inclusion of secondary metal dopants, defects in the structure, and metal-support interactions [10–12]. One of the efficient strategies to provide higher concentration of oxygen vacancies in the CeO_2 structure is by metal-support interactions that occur by anchoring CeO_2 over a metal oxide (SiO_2, Al_2O_3, ZnO, and others) by impregnation, hydrothermal, sol–gel process, electrodeposition and metal precursor hydrolysis [8,13–20].

In this paper, we describe a simple approach for the synthesis of CeO_2 supported on SiO_2 catalysts obtained by two different methods: (i) CeO_2–MCM-41 obtained by the in situ incorporation of a cerium precursor into the mesoporous silica MCM-41 framework, and (ii) CeO_2–SiO_2 obtained by conventional wet impregnation of commercial CeO_2 over SiO_2 and $Ce(NO_3)_3$ over MCM-41. It is important to note that, in the CeO_2 containing MCM-41, the active site-isolation in the framework positions of solid matrices prevents metal aggregation to produce less reactive species [21]. Specifi-

* Corresponding author.
E-mail address: pard@ufmg.br (P.A. Robles-Dutenhefner).

http://dx.doi.org/10.1016/j.cej.2015.10.097
1385-8947/

cally, we were interested in studying how the preparation method of the CeO_2-based catalysts could influence their active site-support interaction, the concentration of oxygen vacancies, and their corresponding catalytic performances towards benzene, toluene, and *o*-xylene (BTX) oxidation. Although these organic compounds are harmful to the atmosphere and human health, they are still released to the environment by a variety of daily activities. Thus, the BTX oxidation was chosen as a model to probe catalytic performances as it represents one of the most important methods to their removal from the environment due to its high degradation efficiency and low energy costs [22–24].

2. Experimental

2.1. Chemicals

All reagents were purchased from commercial sources and used as received.

2.2. Preparation of CeO_2–MCM-41 catalyst by the in situ incorporation of Ce

CeO_2–MCM-41 (1.0, 5.0 and 10 wt%) catalyst was prepared by the in situ incorporation of Ce into the MCM-41 framework. Tetraethyl orthosilicate (TEOS, 99%, Sigma–Aldrich), and $Ce(NO_3)_3{\cdot}6H_2O$ (99%, Sigma–Aldrich) were the precursors and hexadecyltrimethylammonium bromide (CTAB, Sigma–Aldrich) was the structural template. A solution of CTAB in water (4 g/25 mL) was added to a solution of TEOS (2.5 g) in aqueous tetramethylammonium hydroxide (TMAOH, 25 wt%, Sigma–Aldrich), and the mixture was stirred for 30 min. Next, $(CeNO_3)_3{\cdot}6H_2O$ (0.47 g, 2.4 g, and 4.7 g for 1.0, 5.0. and 10 wt% catalysts, respectively), and the remaining TEOS (21.0 g) were added. After additional stirring at 40 °C for 24 h, the mixture was autoclaved at 100 °C for 24 h and then cooled to room temperature. The resulting solid was separated by filtration, washed with deionized water and ethanol and dried at 40 °C. The solid was then heated from room temperature to 550 °C under flowing nitrogen and calcined for 3 h at 550 °C under a flow of air to remove the residual organic compounds. The TEOS/C16-TAB/TMAOH/water molar ratio was 1.0/0.12/0.3/22.0.

2.3. Preparation of CeO_2–MCM-41 obtained by the impregnation of Ce $(NO_3)_3{\cdot}6H_2O$ over MCM-41

Briefly, 126 mg of $Ce(NO_3)_3{\cdot}6H_2O$ was dissolved in 30 mL of deionized H_2O. Then, 1.0 g of pure MCM-41 (obtained by the same protocol above mentioned without the use of $Ce(NO_3)_3{\cdot}6H_2O$) was added to the resulting suspension and vigorously stirred at 80 °C to produce a paste. After that, 50 mL of deionized water was added and the suspension was stirred until completely dry (~5 h). The resulting solids were then treated at 550 °C for 3 h under air.

2.4. Preparation of CeO_2–SiO_2 catalyst by wet impregnation

CeO_2–SiO_2 catalyst was prepared by wet impregnation method. 50 mg of CeO_2 (Riedel-de Haen) were suspended in 30 mL of water. Then, 1 g of SiO_2 (70–230 mesh, VETEC) was added to resulting suspension and vigorously stirred at 80 °C until the formation of a paste. Then, 50 mL of distilled water was added and the suspension was kept under stirring to dryness (~5 h). The resulting solid were then treated at 120 °C for 2 h under air. The solid was then heated from room temperature to 550 °C under a flow of air.

2.5. Catalyst characterization

The catalysts were characterized physically and chemically after calcination.

Powder X-ray diffraction (XRD) patterns were recorded on a Rigaku Geigerflex-3034 diffractometer with Cu$K\alpha$ radiation (40 kV, 40 mA, λ = 0.15418 nm). The Bragg angle (2θ) ranged from 15° to 70°, with a step size of 0.05°, and a step time of 4.0 s. Samples were previously dried at 110 °C overnight and pulverized.

The reducibility of the catalytic surface was determined by Temperature-Programmed Reduction (TPR) in a Quantachrome ChemBET-300 instrument equipped with a thermal conductivity detector. Prior to analysis ca. 150 mg was packed into a quartz cell, heated for 2 h at 200 °C under a stream of pure He and then cooled to room temperature. The experiments were performed between 30 and 900 °C in a flow of 5% H_2/N_2, the temperature increasing linearly at a rate of 10 °C min^{-1}. The O_2-chemisorption was conducted at 600 °C using a ChemBET analyzer (Quantachrome Instruments®).

Micro-Raman spectra were collected using a Renishaw RL633 laser spectrometer. Measurements were performed by using a helium–neon laser (632.8 nm and an effective power of 6 mW at the sample's surface) equipped with a CCD detector, 50× lens, and an experimental resolution of typically 1 μm for 10 accumulations of 20 s.

Textural characteristics of the matrices were determined from nitrogen adsorption isotherms, recorded at −196 °C in an Autosorb IQ – Quantachrome Instrument. The samples (ca. 200 mg) were degassed for 2 h at 300 °C before analysis. Specific surface areas were determined by the Brunauer–Emmett–Teller equation (BET method) from adsorption isotherm generated in a relative pressure range $0.07 < P/P_o < 0.3$. The total pore volume was calculated from the amount of N_2 adsorbed at a relative pressure close to unity. The average pore diameter was determined by the Barrett–Joyner–Halenda (BJH) method from the N_2 desorption isotherms.

Small-angle X-ray scattering (SAXS) was carried out at the D11A-SAXS beam line at the LNLS synchrotron laboratory (Campinas, Brazil), using a Huber-423 three-circle diffractometer. The SAXS setup was equipped with a Si (1 1 1) monochromator, giving a horizontally focused X-ray beam. The incident X-ray wavelength λ was 1.488 nm and the scattering angle 2θ was varied from 0° to 10°.

Transmission electron microscope (TEM) images were taken with a Tecnai-G2-20 (FEI) electron microscope with an acceleration potential of 200 kV. The scanning electron microscopy (SEM) images were obtained using a JEOL field emission gun microscope JSM 6330F operated at 5 kV. The samples were prepared by drop-casting an aqueous suspension containing the nanostructures over a silicon wafer, followed by drying under ambient conditions.

2.6. Benzene, toluene and o-xylene oxidation

The catalytic oxidation of benzene, toluene and *o*-xylene was investigated. The reactions were performed in a fixed-bed tubular quartz reactor under atmospheric pressure. The following conditions were chosen: 0.11 g of catalyst, inlet benzene (>99%, Vetec) concentration 1.2 g m^{-3}, toluene (>99%, Vetec) concentration 0.7 g m^{-3}, *o*-xylene (>99%, Vetec) concentration 0.5 g m^{-3} in air and temperature range 150–400 °C. The reaction data were collected after at least 2 h on stream at room temperature. The reaction products were determined by gas chromatography coupled to mass spectrometry (GC–MS). The reactant and product mixtures were analyzed with two in-line gas chromatographs equipped with FID and TCD detectors and an HP-5 column. The catalytic activity was expressed as the percent conversion of benzene, toluene and

o-xylene, respectively. The conversion of the compounds (benzene, toluene and *o*-xylene) was calculated as follows:

$$\text{CBTXs } (\%) = \frac{[\text{BTXs}]_{in} - [\text{BTXs}]_{out}}{[\text{BTXs}]_{in}} \times 100\%$$

where CBTXs (%) = percent BTX conversion; $[\text{BTXs}]_{in}$ = input quantity and $[\text{BTXs}]_{out}$ = output quantity.

3. Results and discussion

We started our studies by focusing on well-defined CeO_2–MCM-41 materials obtained by the in situ incorporation of the cerium precursor into the mesoporous silica MCM-41 framework. During the synthesis, SiO_2 is evenly distributed in the hexagonal structure of rod-like surfactant micelles of CTAB molecules (cetyltrimethylammonium bromide) to produce the MCM-41 structure [25,26]. In this case, $Ce(NO_3)_3$ (cerium precursor) was also added to the recipe in order to produce CeO_2, together with MCM-41, in the micellar solution of CTAB. It is expected that this approach would lead to catalysts with strong CeO_2–MCM-41 interactions. For the sake of comparison, we also prepared a CeO_2–SiO_2 catalyst by wet impregnation [27] of commercial CeO_2 into SiO_2 in order to investigate the influence of both methods on the structural features and catalytic properties towards the BTX oxidation. Fig. 1 shows the XRD patterns of the CeO_2–MCM-41 and CeO_2–SiO_2. Whereas the diffractogram of CeO_2–SiO_2 indicated four lines corresponding to the (1 1 1), (2 0 0), (2 2 0) and (3 1 1) crystal planes of cubic fluorite (CeO_2) [6], the CeO_2–MCM-41 did not present any well-defined peaks assigned to CeO_2 phases. This observation suggests that the CeO_2 is better dispersed on the in MCM-41 framework relative to commercial silica and may exhibit an improved interaction with the mesoporous silica. The broad peak observed in CeO_2–MCM-41 diffractogram is due to amorphous SiO_2 [28,29].

TPR experiments were performed in order to investigate the redox properties of the prepared catalysts. One broad reduction peak associated with the reduction of Ce^{4+} to Ce^{3+} in the bulk of the CeO_2 was registered in the TPR profiles of both catalysts (Fig. 2) [30–32]. This peak was centered at 864 and 665 °C and for CeO_2–SiO_2 and CeO_2–MCM-41 catalysts, respectively, indicating the higher reducibility for the CeO_2–MCM-41 catalyst. This can be assigned to the high dispersion of CeO_2 and interaction with the MCM-41 support [7,14,33]. In addition, the shift to a lower reduction temperature can also be ascribed to the higher surface CeO_2 concentration and smaller crystallite size presented in this sample, which is consistent with XRD data [6,8,9,14].

O_2-chemisorption measurements also support the XRD and TPR analysis and allowed us to estimate the total amount of oxygen storage capacity (OSC) available in each catalyst, which is related to the number of oxygen vacancies in the samples. The CeO_2–MCM-41 catalyst exhibited a higher density of oxygen sites than CeO_2–SiO_2 catalyst (5.15×10^3 and 3.22×10^3 μmol/m^2 for CeO_2–MCM-41 and CeO_2–SiO_2, respectively), indicating an interaction between CeO_2 and the support as well as the higher oxygen vacancies concentration at the CeO_2–MCM-41 surface [34].

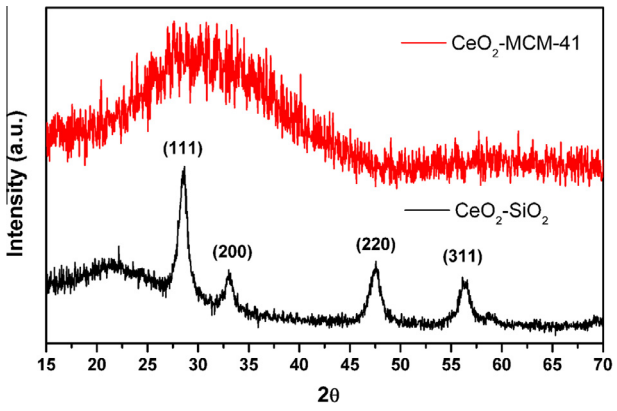

Fig. 1. XRD patterns of CeO_2–MCM-41 and CeO_2–SiO_2.

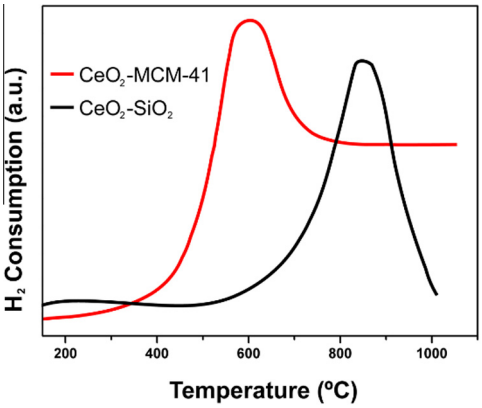

Fig. 2. TPR profiles of CeO_2–MCM-41 and CeO_2–SiO_2.

We also investigated the presence of oxygen vacancies in the CeO_2–SiO_2 and CeO_2–MCM-41 by Raman spectroscopy as shown in Fig. 3A and B. The Raman spectrum (Fig. 3A) of CeO_2–SiO_2 indicated a band centered at 466.4 cm^{-1}, which is assigned to the F_{2g} mode of the fluorite structure (symmetric stretching vibration of the oxygen atoms around Ce^{4+} ions) [6,35]. Interestingly, the F_{2g} mode for the CeO_2–MCM-41 was broadened and shifted to 461.3 cm^{-1}, which suggests the presence of defects on the CeO_2 structure [6,36,37]. We also observed in the Raman spectra of CeO_2–MCM-41 two weak bands in the 540–620 cm^{-1} region corresponding to the non-degenerate LO modes of CeO_2, assigned to the oxygen vacancies introduced into the ceria structure [6,36]. Therefore, our data indicate that CeO_2–MCM-41 presents increased the content of oxygen vacancies relative to the CeO_2–SiO_2 catalyst, which is in agreement with XRD and TPR results.

Surface areas and average pore sizes obtained by BET showed that specific surface area for the CeO_2–MCM-41 catalyst was much higher (727 m^2/g) than CeO_2–SiO_2 (153 m^2/g). The CeO_2–MCM-41 catalysts also displayed a much smaller average BJH pore diameter

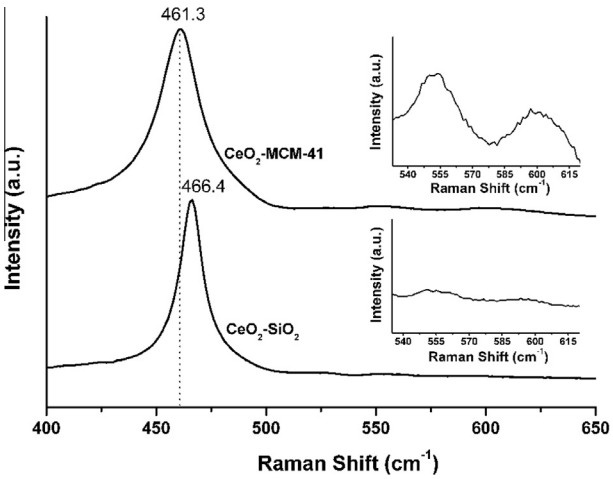

Fig. 3. Raman spectra of CeO_2–MCM-41 and CeO_2–SiO_2 catalysts. The insets present a zoom at the 530–620 cm^{-1} region.

Table 1
Textural properties measured by N_2-physisorption and O_2-chemissortion for the CeO_2-based catalysts.

Catalyst	Density of oxygen sites (μmol/m^2)	Surface area (m^2/g)	Pore volume (cm^3/g)	Pore diameter (Å)
1 wt% CeO_2–MCM-41	2.99×10^3	832	1.0	2.0
5 wt% CeO_2–MCM-41	5.15×10^3	727	0.5	1.9
10 wt% CeO_2–MCM-41	3.89×10^3	169	0.8	2.5
5 wt% CeO_2–SiO_2	3.22×10^3	153	0.7	9.0

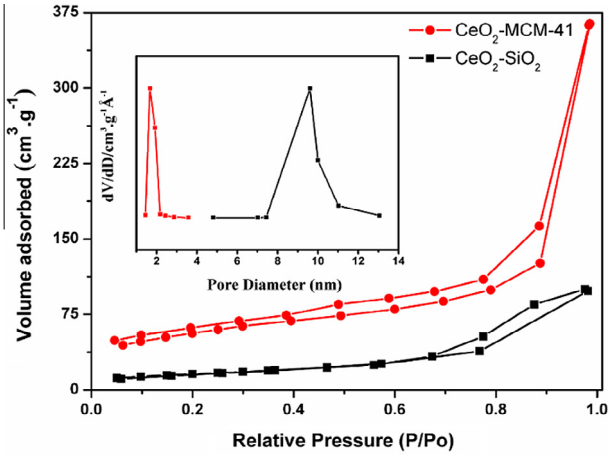

Fig. 4. N_2-adsorption–desorption isotherms of CeO_2–MCM-41 and CeO_2–SiO_2 catalysts and pore size distribution curves (inset) generated by the BJH method from the N_2 desorption isotherms.

(1.9 nm) relative to CeO_2–SiO_2 (9 nm). These results are depicted in Table 1. The isotherm for CeO_2–SiO_2 catalyst (Fig. 4) corresponds to type IV (IUPAC classification), which is typical of mesoporous materials. The shape of the hysteresis loop type H1 appeared at relative pressures $P/P_o \approx 0.9$–1.0 and could be related to the formation of textural mesoporosity [38]. The CeO_2–MCM-41 exhibited a type IV isotherm (Fig. 4) (IUPAC classification), with well-defined H3 loops that did not level off at relative pressures close to the saturation vapor pressure, as reported for aggregates of plate-like particles giving rise to slit-shaped pores. Thus, the high BET surface areas, type IV nitrogen adsorption–desorption isotherm, and narrow pore size distribution confirm the uniform mesoporosity and ordered structure of the CeO_2–MCM-41 material.

The ordered hexagonal structure of CeO_2–MCM-41 was further confirmed by HRTEM image (Fig. 5A), showing the hexagonal arrangement of uniform pores (inset of Fig. 5A). The HRTEM results also revels the absence of individual, small CeO_2 aggregates, which agrees with XRD results and indicate that cerium could be successfully incorporated into the MCM-41 structure. On the other hand, the TEM image of CeO_2–SiO_2 catalyst (Fig. 5B) showed the presence of elongated and irregular particles of CeO_2 and SiO_2. Also, the mass-thickness contrast detected from the TEM image indicates that SiO_2 and CeO_2 particles were directly connected (Fig. 5B).

The structure of CeO_2–MCM-41 was also studied by SAXS. The synchrotron radiation small-angle pattern for the CeO_2–MCM-41 (Fig. 6) showed (1 0 0), (1 1 0) and (2 0 0) reflections at $2\theta = 1.67°$, 2.91°, and 3.33°, respectively. These reflections can be attributed to the 2-D hexagonal symmetry that is typical of the MCM-41 ordered hexagonal structure [25]. Therefore, these results indicated that in situ CeO_2 generation during the synthesis of MCM-41 did not prevent the formation of ordered mesoporous silica, which agree with HRTEM data.

The catalytic activity of the CeO_2–MCM-41 and CeO_2–SiO_2 samples was examined towards the oxidation of BTX compounds. We were interested in investigating how the catalytic performances

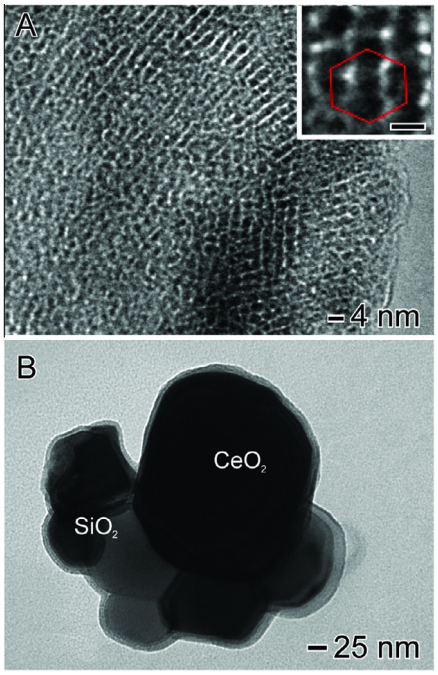

Fig. 5. HRTEM (A) and TEM (B) images of CeO_2–MCM-41 and CeO_2–SiO_2 catalysts, respectively. The scale bar the inset corresponds to 2 nm.

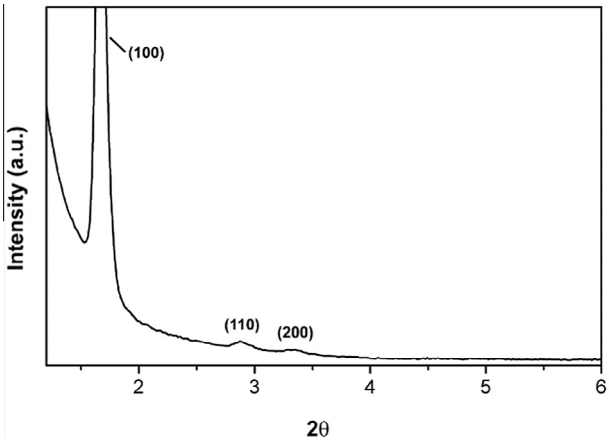

Fig. 6. SAXS pattern of CeO_2–MCM-41 catalyst.

of the CeO_2–MCM-41 and CeO_2–SiO_2 towards BTX oxidation were dependent upon their physicochemical properties. Fig. 7A–C depicts the conversion percentages for the oxidation of benzene (Fig. 7A), toluene (Fig. 7B), and *o*-xylene (Fig. 7C) as a function of reaction temperature employing CeO_2–MCM-41 and CeO_2–SiO_2 as catalysts. The inset in Fig. 6A–C shows the TOF_{max} at maximum conversion of BTX. From Fig. 7A–C, it can be observed a significant difference regarding the activities of CeO_2–MCM-41 and CeO_2–SiO_2. While no appreciable conversion was detected for the

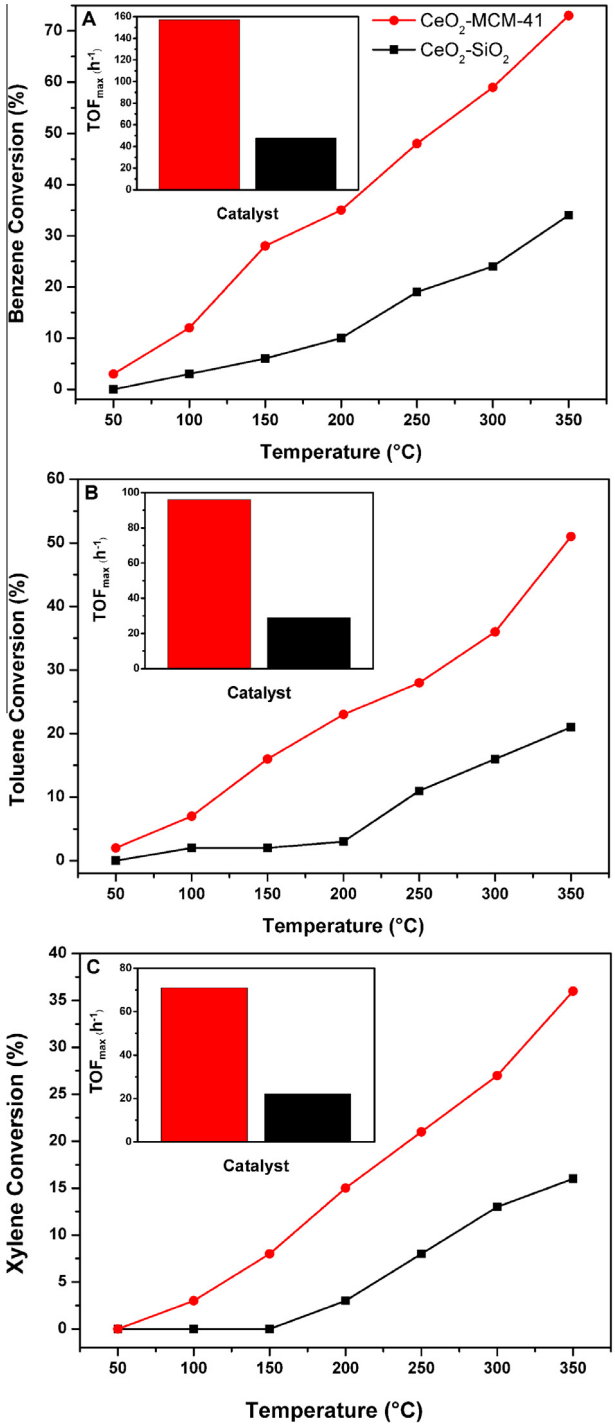

Fig. 7. BTX oxidation expressed as conversion % as a function of temperature catalyzed by CeO_2–MCM-41 and CeO_2–SiO_2.

pure SiO_2 support and CeO_2 (<3%, not shown in the Fig. 7), both CeO_2–MCM-41 and CeO_2–SiO_2 displayed high catalytic activities at relatively low temperatures, showing that the appropriate combination of oxides can provide higher activities relative to their individual counterparts. The oxidation of benzene, toluene and *o*-xylene began to take place at above 60 °C. Only H_2O and CO_2 were detected as the oxidation products, and the BTX conversion increased with temperature for both catalysts. CeO_2–MCM-41 was notably more active than the CeO_2–SiO_2 at the higher temperatures. Specifically, 74% and 33% conversion for benzene, 53% and

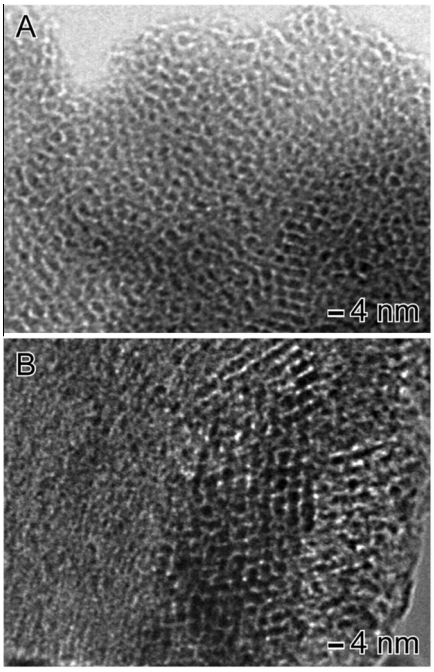

Fig. 8. HRTEM images of the 1 wt% CeO_2–MCM-41 (A) and 10 wt% CeO_2–MCM-41 (B) catalysts.

19% conversion for toluene, and 37% and 15% conversion for *o*-xylene were observed at 350 °C when CeO_2–MCM-41 and CeO_2–SiO_2 were employed as catalysts, respectively. The TOF values followed the same trend corresponding to 157 and 48 h^{-1} for benzene, 96 and 29 h^{-1} for toluene and 72 and 23 h^{-1} for *o*-xylene using CeO_2–MCM-41 and CeO_2–SiO_2 as catalysts, respectively.

Assuming the same CeO_2 content for both catalysts (5 wt%), the higher activities for CeO_2–MCM-41 can be explained due to its higher specific surface area, stronger ceria-support interactions, and higher oxygen vacancy concentrations. In this case, the greater reducibility of CeO_2–MCM-41 was translated into higher oxidation activities [6,8,14]. The high amount of oxygen vacancies can result in an enhancement in the surface oxygen mobility [39]. In oxidation reactions, the catalyst is subjected to cycles of oxidation and reduction, in which both processes are affected by the oxygen mobility of the catalyst. It is a consensus that, when CeO_2 based catalysts are involved, the oxidation of hydrocarbons occurs via the Mars-van Krevelen mechanism in which the solid oxidizes the substrate. Thus, the key steps are the supply of oxygen by the reducible oxide, the introduction of the oxygen species from the lattice oxide into the substrate molecule, and the re-oxidation of the reduced solid by the oxygen-containing gaseous phase, which is the rate-determining step of the reaction [2,9,40,41]. Therefore, the results reported herein indicate that the methodology used to prepare CeO_2–MCM-41 led to the highest active catalyst for BTX oxidation.

We also investigated the influence of CeO_2 content in the ordering of mesoporous structure and its catalytic performance. Fig. 8A and B shows HRTEM images of 1 and 10 wt% CeO_2–MCM-41. As expected, the increase of cerium content on the in situ CeO_2 generation during the MCM-41 synthesis promoted partial disordering of mesoporous silica but it does not prevent the overall formation of the mesoporous structure (Fig. 8B). Both 1 and 5 wt% CeO_2–MCM-41 (Figs. 8A and 5A, respectively) displayed high uniformity, while the sample containing 10 wt% CeO_2 were less uniform. Indeed, this behavior was similar to other reported catalysts [25,26], in which transition metals have been incorporated

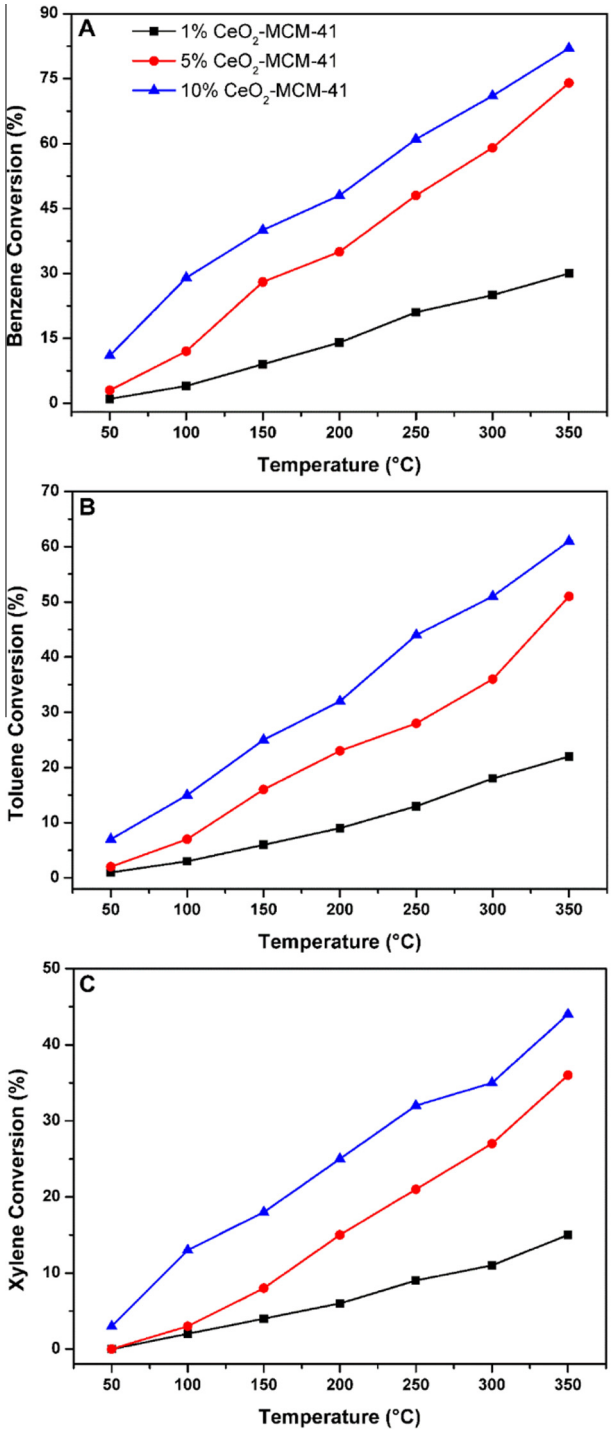

Fig. 9. BTX oxidation expressed as conversion % as a function of temperature catalyzed by 1, 5, and 10 wt% CeO_2–MCM-41.

into the MCM-41 structure by mixing the dissolved metal precursor into the initial solution of TEOS, water, and CTAB. It is plausible that the increase of CeO_2 content did not contribute to the formation of ordered surfactant aggregates, which are uniformly distributed in the hexagonal phase of rod-like surfactant micelles of alkyltrimethylammonium bromide surfactant.

BET and O_2-chemissortion analyses are in agreement with the HRTEM results as depicted in Table 1. A slight decrease of surface area (832–727 m^2/g) and an increase in the density of oxygen sites (2.99 –5.15 μmol/g) were detected when the CeO_2 content was

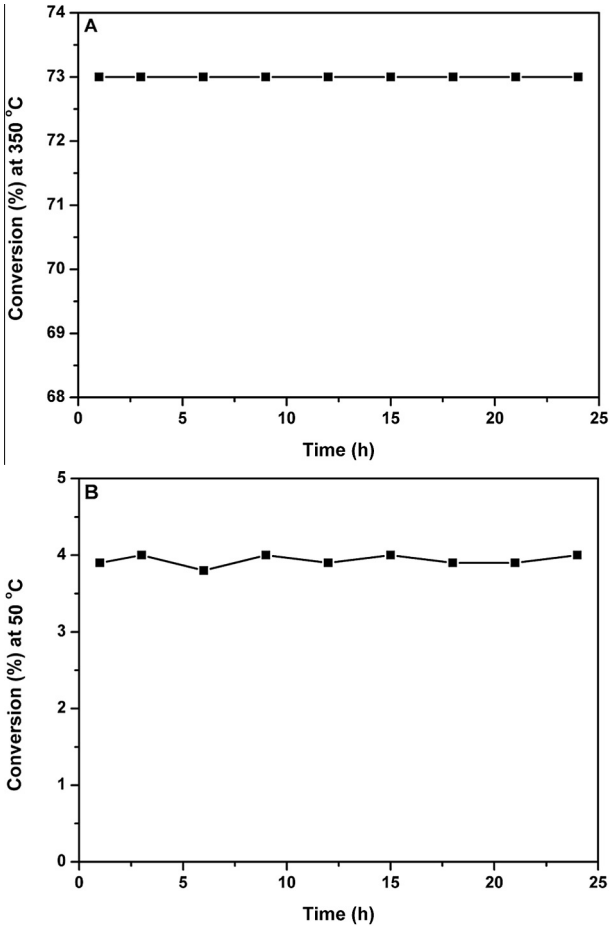

Fig. 10. Benzene conversion percentages as a function of time employing 5 wt% CeO_2–MCM-41 at 50 °C (A) and 350 °C (B) as the reaction temperature.

increased from 1 to 5 wt%. Interestingly, the partial disordering of mesoporous structure observed for the 10 wt% CeO_2–MCM-41 was also accompanied by significant changes in its textural properties, leading to surface areas and density of oxygen sites corresponding to 169 m^2/g and 3.89 × 10^3 μmol/m^2, respectively.

Fig. 9A–C depicts the conversion % for the oxidation of benzene (Fig. 9A), toluene (Fig. 9B), and *o*-xylene (Fig. 9C) as a function of reaction temperature employing 1, 5, and 10 wt% CeO_2–MCM-41 as catalysts, respectively. As expected, BTX conversion % increased with the increase of CeO_2 content, since CeO_2 is the active phase of the catalysts. Although a significant increase of BTX conversion was observed when the CeO_2 content varied from 1 to 5 wt%, this behavior was not obtained for the 10 wt% CeO_2–MCM-41 catalyst. The sample containing 10 wt% CeO_2 was only slightly better than 5 wt% CeO_2–MCM-41 catalyst. Here, it is plausible that the disordering of mesoporous structure observed for the 10 wt% CeO_2–MCM-41 catalyst led to a lower specific surface area, poorer interaction of ceria with the support, and lower concentration of oxygen vacancies in the CeO_2 structure, thus leading to detrimental effects over their catalytic performances.

The catalytic stability towards the benzene oxidation was investigated as a function of time for the 5 wt% Ce/MCM-41 catalyst as shown in Fig. 10. This material was chosen as it corresponds to the sample having the best uniformity, higher concentration of oxygen vacancies, and best textural properties. It can be observed that no significant loss of catalytic activity was detected even after 24 h when the reaction was performed both at 50 and 350 °C. This observation indicates that these materials may represent

Table 2
Oxidation of benzene and toluene over CeO_2/MCM-41 catalysts and other catalysts reported in literature.

Catalyst	T_{BTX50} (°C)	Compound	Reference
CeO_2–SiO_2[a]	>350	BTX	This work
5% CeO_2–MCM-41[a]	252	Benzene	This work
5% CeO_2–MCM-41[a]	348	Toluene	This work
10% CeO_2–MCM-41[a]	215	Benzene	This work
10% CeO_2–MCM-41[a]	290	Toluene	This work
10% CeO_2–MCM-41[a]	>350	*o*-Xylene	This work
CeO_2[b]	>500	Toluene	[42]
AuCeCP[b]	>400	Toluene	[42]
AuCeDP[b]	260	Toluene	[42]
CeO_2 CM[c]	275	Toluene	[43]
MnO_x–CeO_2[d]	270	Toluene	[44]
Co-UVM-7[e]	390	Toluene	[45]
Au/Co-UVM-7[e]	255	Toluene	[45]
Pd/Co_3O_4 (3DL)[f]	232	*o*-Xylene	[46]
Pt/AC800[g]	131	Benzene	[47]
Pt/Al_2O_3[g]	170	Benzene	[47]
V_2O_5/4.37%Au/TiO_2[h]	200	Benzene	[48]

[a] Gas mixture: 341, 199 and 142 ppm benzene, toluene and *o*-xylene in air respectively; GHSV: 12,000 h^{-1}.
[b] Gas mixture: 0.7% v/v toluene, 10 vol.% O_2 in helium; GHSV: 7.6×10^{-3} mol $(h\ g_{cat})^{-1}$.
[c] Gas mixture: 600 ppm toluene, 20 vol.% O_2 in helium, flow rate of 50 mL min^{-1}.
[d] Gas mixture: 200 ppm benzene, 20 vol.% O_2 in helium; GHSV: 30 mL $(h\ g_{cat})^{-1}$.
[e] Gas mixture: 1000 vppm in air; flow rate: 50 mL min^{-1}.
[f] Gas mixture: 150 ppm in air; flow rate: 100 mL min^{-1}.
[g] Gas mixture: 1000 vppm in air; VHSV: 21,500 h^{-1}.
[h] Gas mixture: 1206 vppm in air; VHSV: 21,500 h^{-1}.

promising candidates for gas-phase catalytic applications. It important to note that the observed conversion at low temperature (50 °C) could not be assigned to an adsorption effect, as the chromatograms collected during the reaction at different temperatures clearly shows the substrate conversion and the concomitant appearing of CO_2 as the reaction product (Fig. S1). In order to demonstrate that our reported approach for the synthesis of CeO_2/MCM-41 prepared by the in-situ incorporation of cerium precursor during the MCM-41 formation was effective for the production of optimized catalysts, their performance was also compared with those from a CeO_2/MCM-41 obtained by impregnation of cerium nitrate precursor over MCM-41 support as depicted in Fig. S2 under the same metal loading (5 wt%). It can be observed that BTX conversion % employing the 5 wt% CeO_2/MCM-41 catalyst (Fig. S3) obtained by wet impregnation were significantly lower than the 5 wt% CeO_2/MCM-41 catalyst prepared by in-situ incorporation of cerium precursor during the MCM-41 formation. Its performance was also compared with other catalysts reported in the literature as depicted in Table 2 [42–48]. It important to note that some catalytic results regarding the BTX oxidation are dependent on the employed operating conditions, including nature of the organic compound, reaction mixture composition, overall gas flow rate, and type of the reactor [22–24]. Moreover, most of reported ceria-based catalysts are employed combining other highly active phases such as noble metals or metal oxides (Pd, Pt, Co, Mn, V_2O_5, among others, Table 2). In this paper, silica (an inert phase) was studies as the support in order to focus on the contribution of CeO_2. Regarding the CeO_2–MCM-41 catalysts, which presented the highest activity, the T_{50} (temperature for the 50% organic compound conversion) was higher relative to other reported catalysts. It is interesting to note that the $T_{Benzene50}$ of 10 wt% CeO_2–MCM-41 was higher than Pt-based catalysts and comparable to the value of the V_2O_5/4.37%Au/TiO_2. Besides, the $T_{Toluene50}$ corresponded to 348 °C over 5%CeO_2–MCM-41 and 300 °C over 10%CeO_2–MCM-41 whereas this value was 390 °C over Co-UVM-7. These observations indicate that the CeO_2–MCM-41 catalytic systems can be considered as efficient catalysts for the BTX oxidation. We believe the approach described herein not only enables the synthesis of CeO_2 catalysts in less steps relative to conventional wet impregnation, but also lead to materials with improved activities towards the BTX oxidation.

4. Conclusion

The CeO_2–MCM-41 catalyst prepared by the in situ impregnation of a cerium precursor during the MCM-41 synthesis presented improved catalytic performance relative the CeO_2–SiO_2 catalyst prepared by the conventional wet impregnation. The higher catalytic activity was a result of its higher specific surface area, improved interaction between ceria and the support, facilitated Ce^{4+}/Ce^{3+} redox process, and higher concentration of oxygen vacancies at the CeO_2 surface, which benefits the migration of oxygen species across its structure and thus oxidation activity. Indeed, our results demonstrated that the method of preparation strongly affects the dispersion/incorporation of the CeO_2 into SiO_2, which can be put to work to yield improved catalytic performances.

Acknowledgements

Financial support from CNPq, CAPES, FAPESP, and FAPEMIG (Brazil) is gratefully acknowledged.

Appendix A. Supplementary data

Supplementary data associated with this article can be found, in the online version, at http://dx.doi.org/10.1016/j.cej.2015.10.097.

References

[1] J.Y.Z. Chiou, J.-Y. Siang, S.-Y. Yang, K.-F. Ho, C.-L. Lee, C.-T. Yeh, et al., Pathways of ethanol steam reforming over ceria-supported catalysts, Int. J. Hydrogen Energy 37 (2012) 13667–13673.
[2] N. Guillén-Hurtado, A. García-García, A. Bueno-López, Isotopic study of ceria-catalyzed soot oxidation in the presence of NO_x, J. Catal. 299 (2013) 181–187.
[3] M. Cargnello, V.V.T. Doan-Nguyen, T.R. Gordon, R.E. Diaz, E.A. Stach, R.J. Gorte, et al., Control of metal nanocrystal size reveals metal-support interface role for ceria catalysts, Science 341 (2013) 771–773.
[4] Y. Wang, F. Wang, Q. Song, Q. Xin, S. Xu, J. Xu, Heterogeneous ceria catalyst with water-tolerant lewis acidic sites for one-pot synthesis of 1,3-diols via Prins condensation and hydrolysis reactions, J. Am. Chem. Soc. 135 (2013) 1506–1515.
[5] T.X.T. Sayle, M. Cantoni, U.M. Bhatta, S.C. Parker, S.R. Hall, G. Möbus, et al., Strain and architecture-tuned reactivity in ceria nanostructures; enhanced catalytic oxidation of CO to CO_2, Chem. Mater. 24 (2012) 1811–1821.
[6] A.G.M. Silva, T.S. Rodrigues, A. Dias, H.V. Fajardo, R.F. Goncalves, M. Godinho, et al., $Ce_{1-x}Sm_xO_{1.9-\delta}$ nanoparticles obtained by microwave-assisted hydrothermal processing: an efficient application for catalytic oxidation of α-bisabolol, Catal. Sci. Technol. 4 (2014) 814–821.
[7] M. Nolan, S.C. Parker, G.W. Watson, The electronic structure of oxygen vacancy defects at the low index surfaces of ceria, Surf. Sci. 595 (2005) 223–232.
[8] J. Vecchietti, A. Bonivardi, W. Xu, D. Stacchiola, J.J. Delgado, M. Calatayud, et al., Understanding the role of oxygen vacancies in the water gas shift reaction on ceria-supported platinum catalysts, ACS Catal. 4 (2014) 2088–2096.
[9] J.M. López, A.L. Gilbank, T. García, B. Solsona, S. Agouram, L. Torrente-Murciano, The prevalence of surface oxygen vacancies over the mobility of bulk oxygen in nanostructured ceria for the total toluene oxidation, Appl. Catal., B 174–175 (2015) 403–412.
[10] R. Zhang, L. Guo, C. Chen, J. Chen, A. Chen, X. Zhao, et al., The role of Mn doping in CeO_2 for catalytic synthesis of aliphatic carbamate from CO_2, Catal. Sci. Technol. (2015).
[11] J.S. Moura, J. da S.L. Fonseca, N. Bion, F. Epron, T. de F. Silva, C.G. Maciel, et al., Effect of lanthanum on the properties of copper, cerium and zirconium catalysts for preferential oxidation of carbon monoxide, Catal. Today 228 (2014) 40–50.
[12] M. Hatanaka, N. Takahashi, T. Tanabe, Y. Nagai, K. Dohmae, Y. Aoki, et al., Ideal Pt loading for a Pt/CeO_2-based catalyst stabilized by a Pt–O–Ce bond, Appl. Catal., B 99 (2010) 336–342.
[13] J.L. Ayastuy, A. Iglesias-González, M.A. Gutiérrez-Ortiz, Synthesis and characterization of low amount tin-doped ceria ($Ce_XSn_{1-X}O_{2-\delta}$) for catalytic CO oxidation, Chem. Eng. J. 244 (2014) 372–381.
[14] O.H. Laguna, A. Pérez, M.A. Centeno, J.A. Odriozola, Synergy between gold and oxygen vacancies in gold supported on Zr-doped ceria catalysts for the CO oxidation, Appl. Catal., B 176–177 (2015) 385–395.

[15] A.I. Carrillo, E. Serrano, J.C. Serrano-Ruiz, R. Luque, J. Garcia-Martinez, Helical Al- and Ce-MCM-41 materials as novel catalyst for acid and redox processes, Appl. Catal., A 435–436 (2012) 1–9.
[16] A.M. Akondi, R. Trivedi, B. Sreedhar, M.L. Kantam, S. Bhargava, Cerium-containing MCM-41 catalyst for selective oxidative arene cross-dehydrogenative coupling reactions, Catal. Today 198 (2012) 35–44.
[17] S. Gnanam, V. Rajendran, Synthesis of CeO_2 or α-Mn_2O_3 nanoparticles via sol–gel process and their optical properties, J. Sol-Gel Sci. Technol. 58 (2011) 62–69.
[18] C. Tyrsted, K.M. Ørnsbjerg Jensen, E.D. Bøjesen, N. Lock, M. Christensen, S.J.L. Billinge, et al., Understanding the formation and evolution of ceria nanoparticles under hydrothermal conditions, Angew. Chem. 124 (2012) 9164–9167.
[19] R. Inguanta, S. Piazza, C. Sunseri, Template electrosynthesis of CeO_2 nanotubes, Nanotechnology 18 (2007) 485605.
[20] A. Gurbani, J.L. Ayastuy, M.P. González-Marcos, J.E. Herrero, J.M. Guil, M.A. Gutiérrez-Ortiz, Comparative study of CuO–CeO_2 catalysts prepared by wet impregnation and deposition–precipitation, Int. J. Hydrogen Energy 34 (2009) 547–553.
[21] I.W.C.E. Arends, R.A. Sheldon, Activities and stabilities of heterogeneous catalysts in selective liquid phase oxidations: recent developments, Appl. Catal., A 212 (2001) 175–187.
[22] W.B. Li, J.X. Wang, H. Gong, Catalytic combustion of VOCs on non-noble metal catalysts, Catal. Today 148 (2009) 81–87.
[23] F.I. Khan, A.Kr. Ghoshal, Removal of volatile organic compounds from polluted air, J. Loss Prev. Process Ind. 13 (2000) 527–545.
[24] L.F. Liotta, Catalytic oxidation of volatile organic compounds on supported noble metals, Appl. Catal., B 100 (2010) 403–412.
[25] A.G.M. da Silva, H.V. Fajardo, R. Balzer, L.F.D. Probst, A.S.P. Lovón, J.J. Lovón-Quintana, et al., Versatile and efficient catalysts for energy and environmental processes: mesoporous silica containing Au, Pd and Au–Pd, J. Power Sources 285 (2015) 460–468.
[26] P.A. Robles-Dutenhefner, K.A. da Silva Rocha, E.M.B. Sousa, E.V. Gusevskaya, Cobalt-catalyzed oxidation of terpenes: Co-MCM-41 as an efficient shape-selective heterogeneous catalyst for aerobic oxidation of isolongifolene under solvent-free conditions, J. Catal. 265 (2009) 72–79.
[27] S.P. Jiang, A review of wet impregnation—an alternative method for the fabrication of high performance and nano-structured electrodes of solid oxide fuel cells, Mater. Sci. Eng., A 418 (2006) 199–210.
[28] M.G. Speziali, A.G.M. da Silva, D.M.V. de Miranda, A.L. Monteiro, P.A. Robles-Dutenhefner, Air stable ligandless heterogeneous catalyst systems based on Pd and Au supported in SiO_2 and MCM-41 for Suzuki–Miyaura cross-coupling in aqueous medium, Appl. Catal., A 462–463 (2013) 39–45.
[29] A.M. da Silva, P. Robles-Dutenhefner, A. Dias, H. Fajardo, A.P. Lovón, J. Lovón-Quintana, et al., Gold, palladium and gold–palladium supported on silica catalysts prepared by sol–gel method: synthesis, characterization and catalytic behavior in the ethanol steam reforming, J. Sol-Gel Sci. Technol. 67 (2013) 273–281.
[30] K. Krishna, A. Bueno-López, M. Makkee, J.A. Moulijn, Potential rare earth modified CeO_2 catalysts for soot oxidation: I. Characterisation and catalytic activity with O_2, Appl. Catal., B 75 (2007) 189–200.
[31] N. Sutradhar, A. Sinhamahapatra, S. Pahari, M. Jayachandran, B. Subramanian, H.C. Bajaj, et al., Facile low-temperature synthesis of ceria and samarium-doped ceria nanoparticles and catalytic allylic oxidation of cyclohexene, J. Phys. Chem. C 115 (2011) 7628–7637.
[32] S. Mandal, K.K. Bando, C. Santra, S. Maity, O.O. James, D. Mehta, et al., Sm-CeO_2 supported gold nanoparticle catalyst for benzyl alcohol oxidation using molecular O_2, Appl. Catal., A 452 (2013) 94–104.
[33] L. Živković, V. Lair, O. Lupan, A. Ringuedé, Effect of samarium addition and annealing on the properties of electrodeposited ceria thin films, Thin Solid Films 519 (2011) 3538–3543.
[34] R. Balzer, L.F.D. Probst, V. Drago, W.H. Schreiner, H.V. Fajardo, Catalytic oxidation of volatile organic compounds (*n*-hexane, benzene, toluene, *o*-xylene) promoted by cobalt catalysts supported on Al_2O_3–CeO_2, Braz. J. Chem. Eng. 31 (2014) 757–769.
[35] B.M. Reddy, A. Khan, P. Lakshmanan, M. Aouine, S. Loridant, J.-C. Volta, Structural characterization of nanosized CeO_2–SiO_2, CeO_2–TiO_2, and CeO_2–ZrO_2 catalysts by XRD, Raman, and HREM techniques, J. Phys. Chem. B 109 (2005) 3355–3363.
[36] B.M. Reddy, A. Khan, Y. Yamada, T. Kobayashi, S. Loridant, J.-C. Volta, Surface characterization of CeO_2/SiO_2 and $V_2O_5/CeO_2/SiO_2$ catalysts by Raman, XPS, and other techniques, J. Phys. Chem. B 106 (2002) 10964–10972.
[37] B.M. Reddy, P. Lakshmanan, A. Khan, Investigation of surface structures of dispersed V_2O_5 on CeO_2–SiO_2, CeO_2–TiO_2, and CeO_2–ZrO_2 mixed oxides by XRD, Raman, and XPS techniques, J. Phys. Chem. B 108 (2004) 16855–16863.
[38] A. Corma, From microporous to mesoporous molecular sieve materials and their use in catalysis, Chem. Rev. 97 (1997) 2373–2420.
[39] S. Todorova, A. Naydenov, H. Kolev, K. Tenchev, G. Ivanov, G. Kadinov, Effect of Co and Ce on silica supported manganese catalysts in the reactions of complete oxidation of *n*-hexane and ethyl acetate, J. Mater. Sci. 46 (2011) 7152–7159.
[40] C. Fang, D. Zhang, L. Shi, R. Gao, H. Li, L. Ye, et al., Highly dispersed CeO_2 on carbon nanotubes for selective catalytic reduction of NO with NH_3, Catal. Sci. Technol. 3 (2013) 803–811.
[41] S. Todorova, G. Kadinov, K. Tenchev, A. Caballero, J.P. Holgado, R. Pereñíguez, Co_3O_4 + CeO_2/SiO_2 catalysts for *n*-hexane and CO oxidation, Catal. Lett. 129 (2009) 149–155.
[42] S. Scirè, S. Minicò, C. Crisafulli, C. Satriano, A. Pistone, Catalytic combustion of volatile organic compounds on gold/cerium oxide catalysts, Appl. Catal., B 40 (2003) 43–49.
[43] D. Delimaris, T. Ioannides, VOC oxidation over MnO_x–CeO_2 catalysts prepared by a combustion method, Appl. Catal., B 84 (2008) 303–312.
[44] X. Tang, Y. Xu, W. Shen, Promoting effect of copper on the catalytic activity of MnO_x–CeO_2 mixed oxide for complete oxidation of benzene, Chem. Eng. J. 144 (2008) 175–180.
[45] B. Solsona, M. Pérez-Cabero, I. Vázquez, A. Dejoz, T. García, J. Álvarez-Rodríguez, et al., Total oxidation of VOCs on Au nanoparticles anchored on Co doped mesoporous UVM-7 silica, Chem. Eng. J. 187 (2012) 391–400.
[46] Y. Wang, C. Zhang, F. Liu, H. He, Well-dispersed palladium supported on ordered mesoporous Co_3O_4 for catalytic oxidation of *o*-xylene, Appl. Catal., B 142–143 (2013) 72–79.
[47] J.C.-S. Wu, Z.-A. Lin, F.-M. Tsai, J.-W. Pan, Low-temperature complete oxidation of BTX on Pt/activated carbon catalysts, Catal. Today 63 (2000) 419–426.
[48] V. Idakiev, L. Ilieva, D. Andreeva, J.L. Blin, L. Gigot, B.L. Su, Complete benzene oxidation over gold-vanadia catalysts supported on nanostructured mesoporous titania and zirconia, Appl. Catal., A 243 (2003) 25–39.